

# Spin-dependent dark matter interactions at loop-level in Ar and Xe

Nassim Bozorgnia,<sup>a,b</sup> Muping Chen,<sup>c</sup> and Graciela B. Gelmini<sup>c</sup>

<sup>a</sup>Department of Physics, University of Alberta,  
Edmonton, Alberta T6G 2E1, Canada

<sup>b</sup>Theoretical Physics Institute, University of Alberta,  
Edmonton, Alberta T6G 2E1, Canada

<sup>c</sup>Department of Physics and Astronomy, UCLA,  
475 Portola Plaza, Los Angeles, CA 90095, USA

E-mail: [nbozorgnia@ualberta.ca](mailto:nbozorgnia@ualberta.ca), [mpchen@physics.ucla.edu](mailto:mpchen@physics.ucla.edu),  
[gelmini@physics.ucla.edu](mailto:gelmini@physics.ucla.edu)

**Abstract.** Xenon and argon are the two noble gases used in tonne scale dark matter direct detection experiments. We compare the detection capability of both target elements for interactions due to a pseudoscalar mediator including loop-level contributions to the cross section. At tree-level this type of interaction depends on the nuclear spin and would thus not be detectable in argon-based detectors, since Ar has spin zero. However, at the loop-level the same interaction yields spin-independent contributions that would be detectable in an argon target and are not negligible with respect to the tree-level interactions in xenon, because these are momentum suppressed. In fact, the loop-level contributions are also important for xenon-based experiments at low recoil energies, which could change their discovery reach for this interaction.

---

## Contents

<b>1</b>	<b>Introduction</b>	<b>1</b>
<b>2</b>	<b>The interaction model</b>	<b>2</b>
<b>3</b>	<b>Loop-level corrections</b>	<b>3</b>
<b>4</b>	<b>Direct detection rates</b>	<b>4</b>
<b>5</b>	<b>Comparison of Ar and Xe detection capability</b>	<b>6</b>
<b>6</b>	<b>Conclusions</b>	<b>9</b>

---

## 1 Introduction

Direct dark matter (DM) detection attempts to detect the energy deposited by the collision of a DM particle from the dark halo of our galaxy within a detector. Xenon (see e.g. [1–7]) and argon (see e.g. [8–13]) are the two liquefied noble gases used in tonne scale direct detection experiments. The proposed 40 tonne (50 tonne total) DARWIN [14], 60 tonne (75 tonne total) XLZD [7] and 43 tonne (47 tonne total) PandaX-xT [6] DM direct detection experiments with liquid xenon, and 300 tonne Global Argon Dark Matter Collaboration (GADMC) consortium ARGO detector [15, 16] with liquid argon, will reach the sensitivity at which the interactions from coherent elastic neutrino-nucleus scattering – the “neutrino fog” – will become the most important background.

The best search strategy in direct DM detection is to cast as wide a net as possible in terms of DM-nucleus interactions (see e.g. ref. [17]). Because the argon nucleus does not have spin, argon-based direct detection experiments are insensitive to all interactions coupling the DM particle to nuclear spin, such as those with axial vector or pseudoscalar mediators at tree-level. Xenon is instead sensitive to these interactions. It is thus important to understand how much of a disadvantage argon-based detectors have with respect to those that are xenon-based to detect this type of interactions. The same interactions that lead to a nuclear spin-dependent cross section at tree-level, at the loop-level always contain terms that are independent of the nuclear spin, and could thus be detected in argon.

Loop-level corrections must include all the particles than can be exchanged within the loop given a particular particle model, and not only the main mediator that is usually sufficient to compute tree-level interactions. These corrections can be computed in a straightforward manner in UV complete particle models. However, we would like instead to extend as little as possible a simplified model consisting of the DM particle and its mediator, the elements needed for tree-level calculations, to preserve its generality. Several calculations exist in this spirit of loop-level corrections to the interactions mediated by a pseudoscalar particle [18–22]. This type of interaction is particularly favorable to produce sizable loop-level contributions to the interaction rate at low recoil energies because at tree-level the cross section is momentum transfer suppressed (see e.g. table 1 and eqs. (2.31) and (2.33) of ref. [17]). Using these loop-level calculations, here we compare the argon and xenon-based direct detection capabilities of fermionic DM with interactions mediated by a pseudoscalar boson with tree-level couplings  $f\gamma_5 f$  with Standard Model (SM) fermions  $f$ .

The paper is structured as follows. In section 2 we discuss the general interaction model for the DM particle and the SM fermions. In section 3 we discuss the loop-level corrections to the interactions. In section 4 we present the expressions used for the computation of direct detection event rates. In section 5 we present our results on the detection capability of Ar and Xe-based detectors, and we conclude in section 6.

## 2 The interaction model

Models of DM particles with a pseudoscalar mediator have been studied for more than a decade [23–25], and UV complete models including interaction of this type have been studied at colliders (see e.g. [26–31]).

Loop-level contributions to a cross-section depend on all the particles that can be exchanged in a particular theory, not only on the mediator which dominates the interaction at the tree-level. Thus, without postulating a complete model, it is of particular importance at this level to include the necessary couplings of the pseudoscalar mediator to the SM Higgs boson required by gauge invariance [18–22]. When these are included, even working at one-loop level, two-loop diagrams cannot be neglected [21, 22].

Following ref. [22], we assume here a simple model for the interaction of a Dirac fermion DM particle  $\chi$  and SM fermions  $f$  mediated by a spin-zero boson field  $\phi$  with mass  $m_\phi$ . Two different types of Lagrangian terms are assumed: S-PS and PS-PS. Here the first S (scalar) or PS (pseudoscalar) refers to the DM coupling without or with a  $\gamma_5$ , respectively, and the second PS to the SM fermion coupling with a  $\gamma_5$ . These are respectively

$$\mathcal{L}_{\text{S-PS}} = g_\chi \phi \bar{\chi} \chi + g_{\text{SM}} \sum_f \frac{m_f}{v} \phi \bar{f} i \gamma_5 f, \quad (2.1)$$

and

$$\mathcal{L}_{\text{PS-PS}} = g_\chi \phi \bar{\chi} i \gamma_5 \chi + g_{\text{SM}} \sum_f \frac{m_f}{v} \phi \bar{f} i \gamma_5 f, \quad (2.2)$$

where  $v = 246$  GeV is the electroweak vacuum expectation value,  $g_\chi$  and  $(g_{\text{SM}} m_f/v)$  denote the coupling constants of the mediator  $\phi$  to the DM and SM fermions, respectively, and  $m_f$  are the SM fermion masses. The couplings of the new field  $\phi$  to SM fermions are taken to be proportional to the Yukawa-couplings ( $m_f/v$ ), in agreement with the hypothesis of minimal flavour violation [32], which leads to weakened flavor physics constraints on them.

Gauge symmetry requires that  $\phi$  couples to the SM Higgs field in a quartic term in the scalar potential. After the electroweak spontaneous symmetry breaking, this quartic coupling yields the term

$$\mathcal{L}_{\text{int}}^{\text{Higgs}} = \frac{1}{2} \lambda_{\phi h} v h \phi^2, \quad (2.3)$$

where  $h$  is the Higgs boson field. This term is identified in ref. [22] as the most relevant  $\phi$ - $h$  coupling, because other interaction terms involving two Higgs bosons do not give any relevant contribution to the calculation of direct detection signatures. The constant  $\lambda_{\phi h}$  is an additional free parameter of the model, constrained to be  $\lambda_{\phi h} \lesssim 0.01$  when the invisible decays  $h \rightarrow \phi\phi$  are kinematically possible, i.e. when  $m_\phi < m_h/2$  (see fig. 6 of ref. [22]).

The parameters of this simple model are, therefore, five: the mass of the DM particle  $m_\chi$ , the mass of the mediator  $m_\phi$ , and the three coupling constants  $g_\chi$ ,  $g_{\text{SM}}$  and  $\lambda_{\phi h}$ . As explained below, in the following  $m_\phi$  is taken to be smaller than the t quark mass and larger than the b quark mass,  $m_b < m_\phi \ll m_t$ , for consistency of the calculations [22].

Initial	Effective S-S	Effective PS-S	Effective S-PS	Effective PS-PS
S-PS	X	0	X	X
PS-PS	X	X	X	X

**Table 1.** The two initial couplings in eqs. (2.1) and (2.2), shown in the first column, generate at the loop-level an effective low energy Lagrangian with terms proportional to some of the other interactions indicated by an  $X$  [22]. S-S refers to couplings  $(\bar{\chi}\chi\bar{f}f)$  and PS-S to  $(\bar{\chi}\gamma_5\chi\bar{f}f)$ , which are both independent of the nuclear spin.

### 3 Loop-level corrections

The two initial interactions in eqs. (2.1) and (2.2), given in the first column of table 1, generate at the loop-level an effective low energy Lagrangian which contains terms proportional to some of the other possible interactions [22], indicated by an  $X$  in the table. S-S refers to couplings  $[\bar{\chi}\chi\bar{f}f]$  and PS-S to  $[\bar{\chi}\gamma_5\chi\bar{f}f]$ , which are both independent of the nuclear spin. Namely, at the loop-level S-PS interactions generate S-S, S-PS and PS-PS terms, while starting from PS-PS interactions, terms proportional to all four interaction types are produced at the loop-level.

We utilize the effective approach developed in ref. [22] for calculations of two-loop processes contributing to the effective DM-gluon interactions, which can replace the full two-loop calculations. In this approach, the two-loop processes can be decomposed into two one-loop diagrams by first integrating out the top quark, and then the mediator  $\phi$ . In order to apply this approach, we need to take  $m_\phi \ll m_t$ . In this case, ref. [22] shows that their effective approach for the two-loop calculation agrees very well with the full two-loop calculations for all values of  $m_\chi$  (see fig. 4 of ref. [22]), and also that when  $m_\phi > m_b$  the contribution from bottom and charm quarks can be neglected.

After matching the effective DM-quark and effective DM-gluon interactions onto non-relativistic DM-nucleon interactions, the effective Lagrangian can be written as [22],

$$\mathcal{L}_{\chi N}^{\text{eff}} = \left( \mathcal{C}_{\text{eff},N}^{\text{SI}} \bar{\chi}\chi + \mathcal{C}_{\text{eff},N}^{\text{SI,CPV}} \bar{\chi}i\gamma_5\chi \right) \bar{N}N + \left( \mathcal{C}_{\text{eff},N}^{\text{SD,CPV}} \bar{\chi}\chi + \mathcal{C}_{\text{eff},N}^{\text{SD}} \bar{\chi}i\gamma_5\chi \right) \bar{N}i\gamma_5N, \quad (3.1)$$

where  $N = p, n$  indicates proton or neutron fields. The coefficients  $\mathcal{C}_{\text{eff},N}$  are given in ref. [22] and depend on tree-level and loop-level coefficients. The labels ‘‘SI’’ and ‘‘SD’’ refer to nuclear-spin dependent and nuclear-spin independent terms, and the label ‘‘CPV’’ refers to CP violation and is used for coefficients that exist only when CP is violated.

We refer the reader to ref. [22] for detailed expressions of the  $\mathcal{C}_{\text{eff},N}$  coefficients, and only mention here their dependence on the Passarino-Veltman functions  $C_0$  and  $C_2$  [33], as well as the  $X_2$ ,  $Y_2$ , and  $Z$  functions defined in ref. [34],

$$\begin{aligned} \mathcal{C}_{\text{eff},N}^{\text{SI}} &= \mathcal{C}_{\text{eff},N}^{\text{SI}}(\mathcal{C}^{\text{tree}}, C_0, C_2, X_2, Y_2, Z_{00}, Z_{001}, Z_{111}), \\ \mathcal{C}_{\text{eff},N}^{\text{SI,CPV}} &= \mathcal{C}_{\text{eff},N}^{\text{SI,CPV}}(\mathcal{C}^{\text{tree}}, C_0, X_2, Z_{00}, Z_{11}), \\ \mathcal{C}_{\text{eff},N}^{\text{SD}} &= \mathcal{C}_{\text{eff},N}^{\text{SD}}(\mathcal{C}^{\text{tree}}, C_0, X_2), \\ \mathcal{C}_{\text{eff},N}^{\text{SD,CPV}} &= \mathcal{C}_{\text{eff},N}^{\text{SD,CPV}}(\mathcal{C}^{\text{tree}}, C_0, C_2, X_2, Y_2), \end{aligned} \quad (3.2)$$

where

$$\mathcal{C}^{\text{tree}} = \frac{g_\chi g_{\text{SM}}}{vm_\phi^2}. \quad (3.3)$$

For the on-shell condition  $p^2 = m_\chi^2$ , where  $p$  is the DM particle momentum, the functions  $C_0$ ,  $C_2$ ,  $X_2$ ,  $Y_2$ , as well as the  $Z$  functions, only depend on  $m_\chi$  and  $m_\phi$ , and can be calculated using `Package-X` [35, 36] and `CollierLink` [37] (see also appendix A of ref. [22]). Notice that the  $\mathcal{C}_{\text{eff},N}$  coefficients also depend on the nuclear form factors for the quark and gluon contents of the nucleon. For the SD coefficients, the nuclear form factors depend on the momentum  $q = |\vec{q}|$  exchanged between the DM particle and the nucleon, due to contributions from the  $\pi$  and  $\eta$  mesons [38].

In general, the SI coefficients  $\mathcal{C}_{\text{eff},N}^{\text{SI}}$  and  $\mathcal{C}_{\text{eff},N}^{\text{SI,CPV}}$  depend on the five parameters  $m_\chi$ ,  $m_\phi$ ,  $g_\chi$ ,  $g_{\text{SM}}$ , and  $\lambda_{\phi h}$ . The SD coefficients  $\mathcal{C}_{\text{eff},N}^{\text{SD}}$  and  $\mathcal{C}_{\text{eff},N}^{\text{SD,CPV}}$  depend on those same parameters in addition to the momentum transfer  $q$ .

The effective Lagrangian in eq. (3.1) can be parametrized in terms of a set of effective operators in the non-relativistic limit [39–43],

$$\mathcal{L}_{\chi N}^{\text{eff}} \rightarrow \sum_i c_i^N \mathcal{O}_i^N. \quad (3.4)$$

For the model we are considering, only the following four effective operators contribute,

$$\begin{aligned} \mathcal{O}_1^N &= 1_\chi 1_N, \\ \mathcal{O}_6^N &= \left( \vec{S}_\chi \cdot \frac{\vec{q}}{m_N} \right) \left( \vec{S}_N \cdot \frac{\vec{q}}{m_N} \right), \\ \mathcal{O}_{10}^N &= i \vec{S}_N \cdot \frac{\vec{q}}{m_N}, \\ \mathcal{O}_{11}^N &= i \vec{S}_\chi \cdot \frac{\vec{q}}{m_N}, \end{aligned} \quad (3.5)$$

where  $\vec{S}_\chi$  is the DM particle spin,  $\vec{S}_N$  is the nucleon spin, and  $m_N$  is the nucleon mass. The coefficients corresponding to these operators are respectively  $c_1^N = \mathcal{C}_{\text{eff},N}^{\text{SI}}$ ,  $c_6^N = (m_N/m_\chi) \mathcal{C}_{\text{eff},N}^{\text{SD}}$ ,  $c_{10}^N = \mathcal{C}_{\text{eff},N}^{\text{SD,CPV}}$ , and  $c_{11}^N = -(m_N/m_\chi) \mathcal{C}_{\text{eff},N}^{\text{SI,CPV}}$ .

## 4 Direct detection rates

With the operators given in eq. (3.5), we calculate the spin averaged DM-nuclide,  $T$ , transition probability [42],

$$P_{\text{tot},T} = \frac{1}{2j_\chi + 1} \frac{1}{2j_T + 1} \sum_{\text{spins}} |\mathcal{M}_T|^2, \quad (4.1)$$

where  $j_\chi$  and  $j_T$  are the total angular momentum of the DM and the target nucleus respectively and  $\mathcal{M}_T$  is the DM-nucleus scattering amplitude summed over nucleons and computed between nuclear states (defined e.g. in eq. (40) of ref. [42]). This transition probability is then used to calculate the DM-nucleus differential cross-section,

$$\frac{d\sigma_T}{dE_R} = \frac{m_T}{2\pi v^2} P_{\text{tot},T} \quad (4.2)$$

where  $E_R$  denotes the recoil energy of the target nucleus,  $m_T$  is the mass of the target nucleus, and  $\vec{v}$  is the relative velocity between the DM and the target nucleus, with  $v \equiv |\vec{v}|$ . Throughout our calculations, we assume there is no difference between the recoil energy and the observed energy, therefore we do not consider an experimental energy resolution.

In the case that the detector includes multiple nuclides, the differential event rate per unit energy, detector mass, and time is given by

$$\frac{dR}{dE_R} = \sum_T \frac{dR_T}{dE_R} = \sum_T \frac{C_T}{m_T} \frac{\rho_\chi}{m_\chi} \int_{v \geq v_{\min,T}} d^3v \frac{d\sigma_T}{dE_R} v f(\vec{v}, t), \quad (4.3)$$

where the sum is over the different isotopes or target nuclides,  $T$ , present in the detector,  $C_T$  is the mass fraction of  $T$  in the detector,  $\rho_\chi$  is the local DM density, and  $f(\vec{v}, t)$  is the local DM velocity distribution in the Earth's rest frame. The minimum DM speed to produce a recoil energy  $E_R$  in the detector is

$$v_{\min,T} = \frac{q}{2\mu_T} = \sqrt{\frac{m_T E_R}{2\mu_T^2}}, \quad (4.4)$$

where  $\mu_T$  is the DM-target nucleus reduced mass.

We assume the Standard Halo Model [44] for describing the local distribution of DM in the galactic halo. Recent cosmological simulations including both DM and baryons show that the Maxwellian distribution fits well the local DM velocity distribution of Milky Way-like galaxies [45–48]. However, DM from massive satellites such as the Large Magellanic Cloud can significantly impact the high speed tail of the local DM velocity distribution [49–51]. For simplicity, we neglect these effects in this work.

The local DM density is set to  $\rho_\chi = 0.3 \text{ GeV/cm}^3$ . The local DM velocity distribution is modelled as a Maxwell-Boltzmann distribution in the galactic rest frame, and truncated at the local escape speed,  $v_{\text{esc}}$ , from the galaxy,

$$f_{\text{gal}}(\vec{v}) = \frac{1}{N_{\text{esc}}(v_0\sqrt{\pi})^3} \left[ e^{-v^2/v_0^2} - e^{-v_{\text{esc}}^2/v_0^2} \right] \Theta(v_{\text{esc}}^2 - \vec{v}^2), \quad (4.5)$$

where

$$N_{\text{esc}} = \text{erf}(v_{\text{esc}}/v_0) - \frac{2}{\sqrt{\pi}} \left( \frac{v_{\text{esc}}}{v_0} \right) e^{-v_{\text{esc}}^2/v_0^2} \left[ 1 + \frac{2}{3} \left( \frac{v_{\text{esc}}}{v_0} \right)^2 \right]. \quad (4.6)$$

Here,  $v_0$  is the local circular speed, and the velocity distribution is normalized such that  $\int d^3v f_{\text{gal}}(\vec{v}) = 1$ . The second term in the bracket in eq. (4.5) ensures that the velocity distribution falls off smoothly to zero at  $v_{\text{esc}}$ . We take  $v_0 = 235 \text{ km/s}$  based on measurements of galactic masers [52, 53], and  $v_{\text{esc}} = 550 \text{ km/s}$  based on measurements of high velocity stars from the RAVE survey [54].

We transform the DM velocity distribution from the galactic rest frame to the Earth's rest frame,

$$f(\vec{v}, t) = f_{\text{gal}}(\vec{v} + \vec{v}_s + \vec{v}_e(t)), \quad (4.7)$$

where  $\vec{v}_s = \vec{v}_c + \vec{v}_{\text{pec}}$  is the velocity of the Sun in the Galactic rest frame, and  $\vec{v}_e(t)$  is Earth's velocity with respect to the Sun, which we neglect in this work. Here,  $\vec{v}_c$  is the Sun's circular velocity (where we take  $v_c = v_0 = 235 \text{ km/s}$ ), and  $\vec{v}_{\text{pec}} = (11.10, 12.24, 7.25) \text{ km/s}$  [55] is the peculiar velocity of the Sun with respect to the Local Standard of Rest, in galactic coordinates.

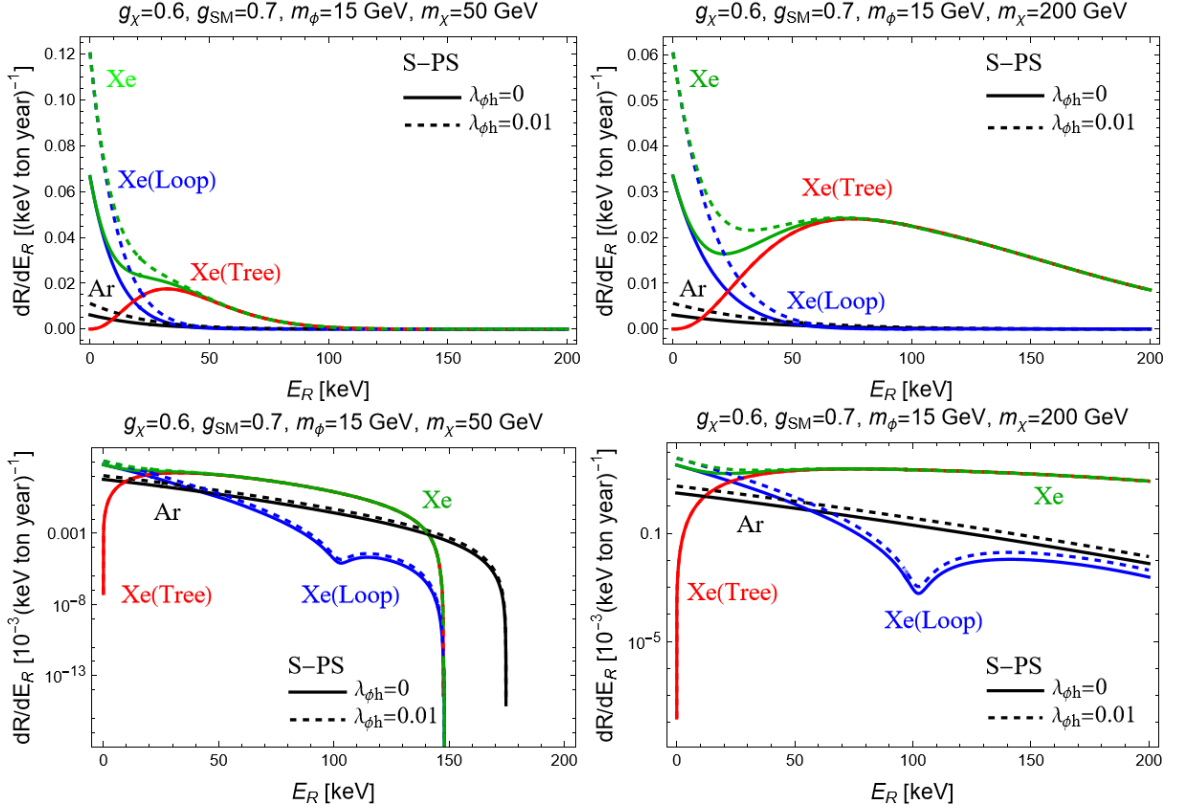


**Figure 1.** Differential event rates for S-PS Lagrangian couplings, with  $g_\chi = 0.6$ ,  $g_{\text{SM}} = 0.7$ ,  $m_\phi = 15$  GeV,  $m_\chi = 50$  GeV (left panels) and  $m_\chi = 200$  GeV (right panels),  $\lambda_{\phi h} = 0$  (solid lines) and  $\lambda_{\phi h} = 0.01$  (dashed lines) for Ar (black lines) and Xe (green lines) targets. The contributions from tree-level only (red lines) and loop-level only (blue lines) in Xe are also shown. The rates are shown in linear scale in the upper panels and in logarithmic scale in the lower panels.

## 5 Comparison of Ar and Xe detection capability

Figures 1 and 2 show the predicted differential event rates for S-PS and PS-PS Lagrangian couplings, respectively, in Ar and Xe targets in linear and logarithmic scales. These figures show the tree-level only (red lines), loop-level contributions only (blue lines) and the total rate (green lines) in Xe, and the total rate entirely due to loop-level contributions (black lines) in Ar targets, for some values of the relevant parameters chosen as examples, i.e.  $m_\phi = 15$  GeV,  $g_\chi = 0.6$ ,  $g_{\text{SM}} = 0.7$ , the minimum and the maximum possible values of the  $\phi$ - $h$  coupling,  $\lambda_{\phi h} = 0$  (solid lines) and  $\lambda_{\phi h} = 0.01$  (dashed lines), and two values of the DM particle mass,  $m_\chi = 50$  GeV and  $m_\chi = 200$  GeV. The event rates have been computed using the Mathematica package `dmformfactor` [42].

Figures 1 and 2 clearly show that the loop-level contributions are important for low recoil energies, and the rates expected for S-PS are much larger, by a factor of about  $10^2$ , than those for PS-PS Lagrangian couplings. In both cases the rates increase with  $\lambda_{\phi h}$ , by a factor of order 1 when going from the minimum to the maximum of this coupling. Also in both cases, even at the lowest recoil energies, the rate expected in an Ar target is smaller by about one order of magnitude than in a Xe target.



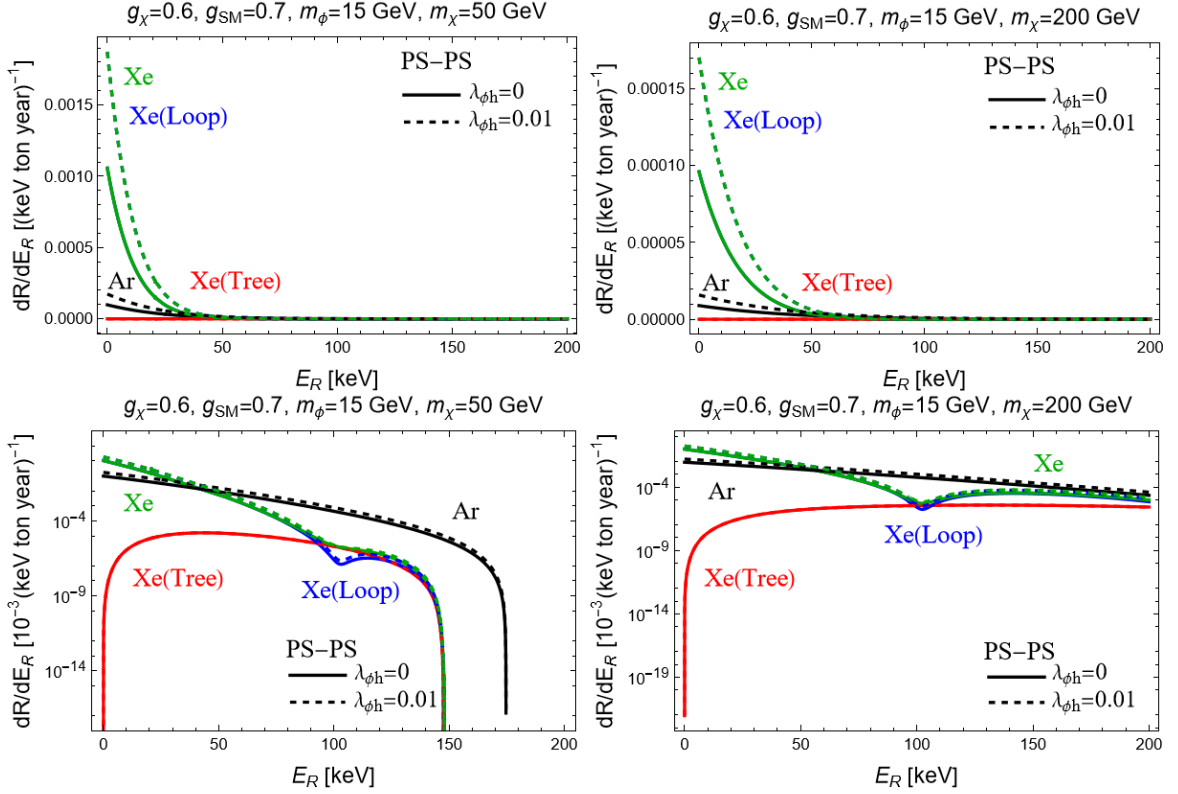


**Figure 2.** Same as fig. 1 but for PS-PS Lagrangian couplings. Notice that the rates are roughly two orders of magnitude smaller than those in fig. 1.

Because loop-level contributions are only important at low energies, the energy threshold of future detectors will be very important to detect rates enhanced by them. Although both argon and xenon-based detectors may achieve nuclear recoil energy thresholds below 1 keV using their S2 (ionization) signal only [10, 12, 56], in fig. 3 we show lines of equal energy-integrated rates taking a threshold of 1 keV for both. This seems a realistic choice for future xenon-based detectors such as DARWIN/XLZD [7] and for argon-based detectors such as DarkSide-LowMass [57]. We consider also the possibility of Ar-based detectors with a larger threshold, such as the 30 keV expected for DarkSide-20k [8] and show the corresponding lines of equal integrated rate in fig. 4.

Figure 3 shows lines of equal integrated rate above the threshold of  $E_R = 1$  keV in the  $g_\chi$ - $m_\chi$  plane, for Ar (left panel) and Xe (right panel) targets, for the most favorable type of Lagrangian coupling of the two we considered, the S-PS. The mediator mass is chosen to be  $m_\phi = 15$  GeV, as in previous figures, and  $\lambda_{ah} = 0$ , which is one of the two values in previous figures. Lines corresponding to an integrated rate of 10 (dot-dashed lines above the solid lines), 1 (solid lines) and 0.1 (dashed lines below the solid lines) in units of  $(\text{ton year})^{-1}$  are given for three different values of the  $g_{\text{SM}}/g_\chi$  coupling ratios, 0.1 (in red), 1 (in black) and 10 (in blue). A few more blue lines corresponding to lower values of integrated rates, as labeled, are given for argon. Notice that we can integrate the total differential event rates (solid lines) in fig. 1 above 1 keV to approximately obtain the value of the black lines in fig. 3 for  $m_\chi = 50$  GeV and 200 GeV,  $g_\chi = 0.7$  and  $g_{\text{SM}}/g_\chi \simeq 1$ .



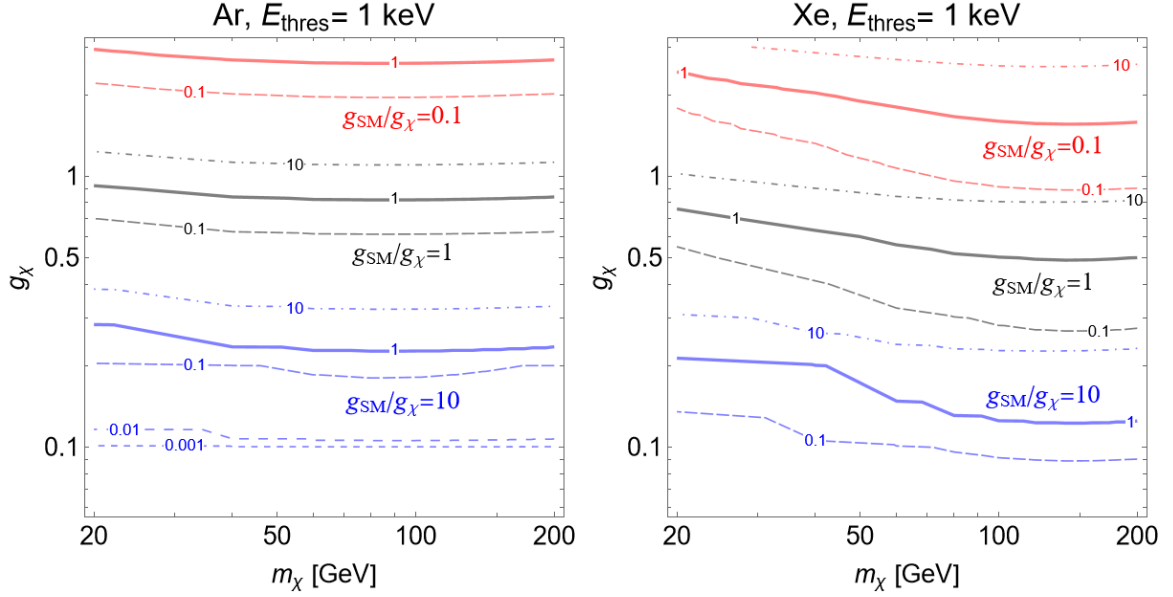


**Figure 3.** Lines of equal energy-integrated event rate for  $E_R > 1$  keV in the  $g_\chi$ - $m_\chi$  plane for Ar (left panel) and Xe (right panel) targets for a model with S-PS Lagrangian couplings,  $m_\phi = 15$  GeV and  $\lambda_{ah} = 0$ , for three different values of the  $g_{\text{SM}}/g_\chi$  coupling ratios, 0.1 (red lines), 1 (black lines) and 10 (blue lines). For each of these ratios different lines are shown corresponding to an integrated rate shown in the respective labels in units of  $(\text{ton year})^{-1}$ , e.g. 10 (dot-dashed lines above the solid lines), 1 (solid lines) and 0.1 (dashed lines below the solid lines).

Figure 3 allows us to estimate the difference in target mass between argon and xenon based detectors required to detect a similar number of events per year, if both have an energy threshold of 1 keV, for two particular values of the parameters. For example, for a 30 GeV DM particle mass,  $g_\chi = 0.2$ , and  $g_{\text{SM}} = 2$ , the blue lines in the left panel show that an integrated rate of  $0.1/(\text{ton year})$  is expected in Ar and the right panel indicates that  $1/(\text{ton year})$  would be expected in Xe. Thus to have a similar rate in both targets one would require a 10 times larger mass in Ar than in Xe. The difference becomes more accentuated for larger DM masses, e.g. for a DM mass of 200 GeV, the rate in argon for the same coupling would still be close to  $0.1/(\text{ton year})$  while in Xe the expected rate is a few events/ $(\text{ton year})$  close to but under  $10/(\text{ton year})$ .

Figure 4 shows lines of equal integrated rate for an Ar target in the  $g_\chi$ - $m_\chi$  plane for the same couplings and parameters used in fig. 3 (i.e. for the S-PS Lagrangian coupling, with  $m_\phi = 15$  GeV and  $\lambda_{ah} = 0$ ), but above the threshold of  $E_R = 30$  keV instead of 1 keV. This figure clearly shows the disadvantage that a larger energy threshold of 30 keV would have to detect DM particle with S-PS couplings in an Ar-based detector. It would make practically impossible for Ar to detect this type of interaction. For example, for a 30 GeV DM particle,  $g_\chi = 0.2$ , and  $g_{\text{SM}} = 2$ , the medium-dashed blue line in fig. 4 shows that an integrated rate of  $0.01/(\text{ton year})$  is expected in Ar. This is an order of magnitude smaller than the rate expected in Ar with an energy threshold of 1 keV for the same couplings.

We do not present specific figures for the integrated rates in the PS-PS case. Our general conclusions comparing both targets would be similar to those for S-PS, but the event rates would be around two orders of magnitude smaller with respect to S-PS, requiring an experimental exposure of  $\sim 100$  times larger to have a signal in the PS-PS case.

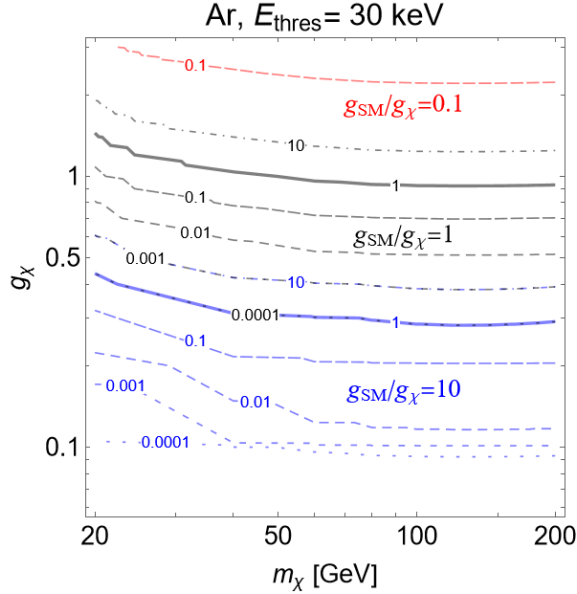


**Figure 4.** Same as figure 3, but only for Ar and assuming an energy threshold of  $E_R = 30$  keV instead of 1 keV. Notice that the solid blue line corresponding to an integrated rate of  $1/(\text{ton year})$  for  $g_{\text{SM}}/g_\chi = 10$  overlays on the dotted black line corresponding to  $0.0001/(\text{ton year})$  for  $g_{\text{SM}}/g_\chi = 1$ .

## 6 Conclusions

In this work we have compared the capability of Ar and Xe based direct detection experiments for detecting fermionic DM candidates with interaction mediated by a spin-zero boson with pseudoscalar couplings to the SM fermions in the Lagrangian. At tree-level this type of coupling depends on the spin of the target nucleus and thus would not be detectable in an argon target, since Ar does not have spin. We considered a minimal extension of the simple one mediator model which allows us to compute loop-level contributions to the direct detection event rate that are independent of the nuclear spin. These contribution are very important at low recoil energies and thus a low energy threshold is essential to detect them.

We showed that with a comparably low energy threshold close to 1 keV, an Ar based detector could have a similar integrated rate as a Xe based detector if its mass is 10 or more times larger than a Xe detector.

These comparisons will be affected by the neutrino fog as shown e.g. in ref. [17] (see figures 3 and 10). The impact of the neutrino fog depends on several factors, such as exposure and interaction type, besides target material. While the loop-level spectrum in Ar is that of a purely spin-independent (SI) interaction, in Xe at high energies the spectrum is purely that of an S-PS coupling, but it deviates significantly from purely S-PS at low energies. Therefore the analysis done in ref. [17] should be redone for Xe for this particular spectrum, which we leave for future work.

## Acknowledgements

NB acknowledges the support of the Natural Sciences and Engineering Research Council of Canada (NSERC), funding reference number RGPIN-2020-07138, the NSERC Discovery Launch Supplement, DGEER-2020-00231, and the Canada Research Chairs Program. MC

and GG were supported in part by the Department of Energy under Award Number DE-SC0009937.

## References

- [1] **XENON** Collaboration, E. Aprile et al., *Constraining the spin-dependent WIMP-nucleon cross sections with XENON1T*, *Phys. Rev. Lett.* **122** (2019), no. 14 141301, [[arXiv:1902.03234](#)].
- [2] **XENON** Collaboration, E. Aprile et al., *Projected WIMP sensitivity of the XENONnT dark matter experiment*, *JCAP* **11** (2020) 031, [[arXiv:2007.08796](#)].
- [3] **LZ** Collaboration, D. S. Akerib et al., *Projected WIMP sensitivity of the LUX-ZEPLIN dark matter experiment*, *Phys. Rev. D* **101** (2020), no. 5 052002, [[arXiv:1802.06039](#)].
- [4] **LZ** Collaboration, D. S. Akerib et al., *The LUX-ZEPLIN (LZ) Experiment*, *Nucl. Instrum. Meth. A* **953** (2020) 163047, [[arXiv:1910.09124](#)].
- [5] **PandaX** Collaboration, H. Zhang et al., *Dark matter direct search sensitivity of the PandaX-4T experiment*, *Sci. China Phys. Mech. Astron.* **62** (2019), no. 3 31011, [[arXiv:1806.02229](#)].
- [6] **PandaX-4T** Collaboration, Y. Meng et al., *Dark Matter Search Results from the PandaX-4T Commissioning Run*, *Phys. Rev. Lett.* **127** (2021), no. 26 261802, [[arXiv:2107.13438](#)].
- [7] L. Baudis, *DARWIN/XLZD: A future xenon observatory for dark matter and other rare interactions*, *Nucl. Phys. B* **1003** (2024) 116473, [[arXiv:2404.19524](#)].
- [8] **DarkSide-20k** Collaboration, C. E. Aalseth et al., *DarkSide-20k: A 20 tonne two-phase LAr TPC for direct dark matter detection at LNGS*, *Eur. Phys. J. Plus* **133** (2018) 131, [[arXiv:1707.08145](#)].
- [9] **ArDM** Collaboration, J. Calvo et al., *Backgrounds and pulse shape discrimination in the ArDM liquid argon TPC*, *JCAP* **12** (2018) 011, [[arXiv:1712.01932](#)].
- [10] **DarkSide-50** Collaboration, P. Agnes et al., *Search for low mass dark matter in DarkSide-50: the bayesian network approach*, *Eur. Phys. J. C* **83** (2023) 322, [[arXiv:2302.01830](#)].
- [11] **DarkSide-20k** Collaboration, I. Manthos, *DarkSide-20k: Next generation Direct Dark Matter searches with liquid Argon*, *PoS EPS-HEP2023* (2024) 113, [[arXiv:2312.03597](#)].
- [12] J. Aalbers et al., *A next-generation liquid xenon observatory for dark matter and neutrino physics*, *J. Phys. G* **50** (2023), no. 1 013001, [[arXiv:2203.02309](#)].
- [13] W. M. Bonivento and F. Terranova, *The science and technology of liquid argon detectors*, [arXiv:2405.01153](#).
- [14] **DARWIN** Collaboration, J. Aalbers et al., *DARWIN: towards the ultimate dark matter detector*, *JCAP* **11** (2016) 017, [[arXiv:1606.07001](#)].
- [15] C. Galbiati, “Direct dark matter detection with noble gases.” Talk at the UCLA Dark Matter 2018 Conference.
- [16] **DarkSide 20k** Collaboration, P. Agnes et al., *Sensitivity of future liquid argon dark matter search experiments to core-collapse supernova neutrinos*, *JCAP* **03** (2021) 043, [[arXiv:2011.07819](#)].
- [17] G. B. Gelmini, V. Takhistov, and S. J. Witte, *Casting a Wide Signal Net with Future Direct Dark Matter Detection Experiments*, *JCAP* **07** (2018) 009, [[arXiv:1804.01638](#)]. [Erratum: *JCAP* **02**, E02 (2019)].
- [18] G. Arcadi, M. Lindner, F. S. Queiroz, W. Rodejohann, and S. Vogl, *Pseudoscalar Mediators: A WIMP model at the Neutrino Floor*, *JCAP* **03** (2018) 042, [[arXiv:1711.02110](#)].

- [19] N. F. Bell, G. Busoni, and I. W. Sanderson, *Loop Effects in Direct Detection*, *JCAP* **08** (2018) 017, [[arXiv:1803.01574](#)]. [Erratum: *JCAP* 01, E01 (2019)].
- [20] T. Li, *Revisiting the direct detection of dark matter in simplified models*, *Phys. Lett. B* **782** (2018) 497–502, [[arXiv:1804.02120](#)].
- [21] T. Abe, M. Fujiwara, and J. Hisano, *Loop corrections to dark matter direct detection in a pseudoscalar mediator dark matter model*, *JHEP* **02** (2019) 028, [[arXiv:1810.01039](#)].
- [22] F. Ertas and F. Kahlhoefer, *Loop-induced direct detection signatures from CP-violating scalar mediators*, *JHEP* **06** (2019) 052, [[arXiv:1902.11070](#)].
- [23] M. Freytsis and Z. Ligeti, *On dark matter models with uniquely spin-dependent detection possibilities*, *Phys. Rev. D* **83** (2011) 115009, [[arXiv:1012.5317](#)].
- [24] K. R. Dienes, J. Kumar, B. Thomas, and D. Yaylali, *Overcoming Velocity Suppression in Dark-Matter Direct-Detection Experiments*, *Phys. Rev. D* **90** (2014), no. 1 015012, [[arXiv:1312.7772](#)].
- [25] C. Boehm, M. J. Dolan, C. McCabe, M. Spannowsky, and C. J. Wallace, *Extended gamma-ray emission from Coy Dark Matter*, *JCAP* **05** (2014) 009, [[arXiv:1401.6458](#)].
- [26] S. Ipek, D. McKeen, and A. E. Nelson, *A Renormalizable Model for the Galactic Center Gamma Ray Excess from Dark Matter Annihilation*, *Phys. Rev. D* **90** (2014), no. 5 055021, [[arXiv:1404.3716](#)].
- [27] J. M. No, *Looking through the pseudoscalar portal into dark matter: Novel mono-Higgs and mono-Z signatures at the LHC*, *Phys. Rev. D* **93** (2016), no. 3 031701, [[arXiv:1509.01110](#)].
- [28] D. Goncalves, P. A. N. Machado, and J. M. No, *Simplified Models for Dark Matter Face their Consistent Completions*, *Phys. Rev. D* **95** (2017), no. 5 055027, [[arXiv:1611.04593](#)].
- [29] M. Bauer, U. Haisch, and F. Kahlhoefer, *Simplified dark matter models with two Higgs doublets: I. Pseudoscalar mediators*, *JHEP* **05** (2017) 138, [[arXiv:1701.07427](#)].
- [30] M. Bauer, M. Klassen, and V. Tenorth, *Universal properties of pseudoscalar mediators in dark matter extensions of 2HDMs*, *JHEP* **07** (2018) 107, [[arXiv:1712.06597](#)].
- [31] **LHC Dark Matter Working Group** Collaboration, T. Abe et al., *LHC Dark Matter Working Group: Next-generation spin-0 dark matter models*, *Phys. Dark Univ.* **27** (2020) 100351, [[arXiv:1810.09420](#)].
- [32] G. D’Ambrosio, G. F. Giudice, G. Isidori, and A. Strumia, *Minimal flavor violation: An Effective field theory approach*, *Nucl. Phys. B* **645** (2002) 155–187, [[hep-ph/0207036](#)].
- [33] G. Passarino and M. J. G. Veltman, *One Loop Corrections for  $e^+ e^-$  Annihilation Into  $\mu^+ \mu^-$  in the Weinberg Model*, *Nucl. Phys. B* **160** (1979) 151–207.
- [34] T. Abe and R. Sato, *Quantum corrections to the spin-independent cross section of the inert doublet dark matter*, *JHEP* **03** (2015) 109, [[arXiv:1501.04161](#)].
- [35] H. H. Patel, *Package-X: A Mathematica package for the analytic calculation of one-loop integrals*, *Comput. Phys. Commun.* **197** (2015) 276–290, [[arXiv:1503.01469](#)].
- [36] H. H. Patel, *Package-X 2.0: A Mathematica package for the analytic calculation of one-loop integrals*, *Comput. Phys. Commun.* **218** (2017) 66–70, [[arXiv:1612.00009](#)].
- [37] A. Denner, S. Dittmaier, and L. Hofer, *Collier: a fortran-based Complex One-Loop Library in Extended Regularizations*, *Comput. Phys. Commun.* **212** (2017) 220–238, [[arXiv:1604.06792](#)].
- [38] F. Bishara, J. Brod, B. Grinstein, and J. Zupan, *From quarks to nucleons in dark matter direct detection*, *JHEP* **11** (2017) 059, [[arXiv:1707.06998](#)].

- [39] J. Fan, M. Reece, and L.-T. Wang, *Non-relativistic effective theory of dark matter direct detection*, *JCAP* **11** (2010) 042, [[arXiv:1008.1591](#)].
- [40] A. L. Fitzpatrick, W. Haxton, E. Katz, N. Lubbers, and Y. Xu, *The Effective Field Theory of Dark Matter Direct Detection*, *JCAP* **02** (2013) 004, [[arXiv:1203.3542](#)].
- [41] A. L. Fitzpatrick, W. Haxton, E. Katz, N. Lubbers, and Y. Xu, *Model Independent Direct Detection Analyses*, [arXiv:1211.2818](#).
- [42] N. Anand, A. L. Fitzpatrick, and W. C. Haxton, *Weakly interacting massive particle-nucleus elastic scattering response*, *Phys. Rev. C* **89** (2014), no. 6 065501, [[arXiv:1308.6288](#)].
- [43] J. B. Dent, L. M. Krauss, J. L. Newstead, and S. Sabharwal, *General analysis of direct dark matter detection: From microphysics to observational signatures*, *Phys. Rev. D* **92** (2015), no. 6 063515, [[arXiv:1505.03117](#)].
- [44] A. K. Drukier, K. Freese, and D. N. Spergel, *Detecting Cold Dark Matter Candidates*, *Phys. Rev. D* **33** (1986) 3495–3508.
- [45] N. Bozorgnia, F. Calore, M. Schaller, M. Lovell, G. Bertone, C. S. Frenk, R. A. Crain, J. F. Navarro, J. Schaye, and T. Theuns, *Simulated milky way analogues: implications for dark matter direct searches*, *JCAP* **05** (2016) 024, [[arXiv:1601.04707](#)].
- [46] C. Kelso, C. Savage, M. Valluri, K. Freese, G. S. Stinson, and J. Bailin, *The impact of baryons on the direct detection of dark matter*, *JCAP* **08** (2016) 071, [[arXiv:1601.04725](#)].
- [47] J. D. Sloane, M. R. Buckley, A. M. Brooks, and F. Governato, *Assessing astrophysical uncertainties in direct detection with galaxy simulations*, *Astrophys. J.* **831** (2016) 93, [[arXiv:1601.05402](#)].
- [48] R. Poole-McKenzie, A. S. Font, B. Boxer, I. G. McCarthy, S. Burdin, S. G. Stafford, and S. T. Brown, *Informing dark matter direct detection limits with the ARTEMIS simulations*, *JCAP* **11** (2020) 016, [[arXiv:2006.15159](#)].
- [49] A. Smith-Orlik et al., *The impact of the Large Magellanic Cloud on dark matter direct detection signals*, *JCAP* **10** (2023) 070, [[arXiv:2302.04281](#)].
- [50] G. Besla, A. Peter, and N. Garavito-Camargo, *The highest-speed local dark matter particles come from the Large Magellanic Cloud*, *JCAP* **11** (2019) 013, [[arXiv:1909.04140](#)].
- [51] K. Donaldson, M. S. Petersen, and J. Peñarrubia, *Effects on the local dark matter distribution due to the large magellanic cloud*, *Mon. Not. Roy. Astron. Soc.* **513** (2022), no. 1 46–51, [[arXiv:2111.15440](#)].
- [52] M. J. Reid et al., *Trigonometric Parallaxes of Massive Star Forming Regions: VI. Galactic Structure, Fundamental Parameters and Non-Circular Motions*, *Astrophys. J.* **700** (2009) 137–148, [[arXiv:0902.3913](#)].
- [53] J. Bovy, D. W. Hogg, and H.-W. Rix, *Galactic masers and the Milky Way circular velocity*, *Astrophys. J.* **704** (2009) 1704–1709, [[arXiv:0907.5423](#)].
- [54] M. C. Smith et al., *The RAVE Survey: Constraining the Local Galactic Escape Speed*, *Mon. Not. Roy. Astron. Soc.* **379** (2007) 755–772, [[astro-ph/0611671](#)].
- [55] R. Schoenrich, J. Binney, and W. Dehnen, *Local Kinematics and the Local Standard of Rest*, *Mon. Not. Roy. Astron. Soc.* **403** (2010) 1829, [[arXiv:0912.3693](#)].
- [56] **DarkSide** Collaboration, P. Agnes et al., *Low-Mass Dark Matter Search with the DarkSide-50 Experiment*, *Phys. Rev. Lett.* **121** (2018), no. 8 081307, [[arXiv:1802.06994](#)].
- [57] **Global Argon Dark Matter** Collaboration, M. Wada, *DarkSide-LowMass: Sensitivity Projections for a New Detector Designed for Light Dark Matter Searches*, *PoS TAUP2023* (2024) 057.